MNRAS 000, 1–6 (2019) Preprint 6 December 2021 Compiled using MNRAS LATEX style file v3.0

Cooling in the shade of warped transition disks

Simon Casassus,[1,2]★ Sebastián Pérez,[1,2,3] Axel Osses,[4] Sebastián Marino,[5]
[1] Departamento de Astronomía, Universidad de Chile, Casilla 36-D, Santiago, Chile
[2] Millennium Nucleus "Protoplanetary Disks", Chile
[3] Universidad de Santiago de Chile, Av. Ecuador 3659, Santiago
[4] Departamento de Ingeniería Matemática, Facultad de Ciencias Físicas y Matemáticas, Universidad de Chile, Beauchef 851, Santiago, Chile
[5] Max Planck Institute for Astronomy, Königstuhl 17, 69117 Heidelberg, Germany

Accepted XXX. Received YYY; in original form ZZZ

ABSTRACT

The mass of the gaseous reservoir in young circumstellar disks is a crucial initial condition for the formation of planetary systems, but estimates vary by orders of magnitude. In some disks with resolvable cavities, sharp inner disk warps cast two-sided shadows on the outer rings; can the cooling of the gas as it crosses the shadows bring constraints on its mass? The finite cooling timescale should result in dust temperature decrements shifted ahead of the optical/IR shadows in the direction of rotation. However, some systems show temperature drops, while others do not. The depth of the drops and the amplitude of the shift depend on the outer disk surface density Σ through the extent of cooling during the shadow crossing time, and also on the efficiency of radiative diffusion. These phenomena may bear observational counterparts, which we describe with a simple one-dimensional model. An application to the HD 142527 disk suggests an asymmetry in its shadows, and predicts a $\gtrsim$10 deg shift for a massive gaseous disk, with peak $\Sigma > 8.3\,\mathrm{g\,cm^{-2}}$. Another application to the DoAr 44 disk limits the peak surface density to $\Sigma < 13\,\mathrm{g\,cm^{-2}}$.

Key words: protoplanetary discs — accretion, accretion discs

1 INTRODUCTION

Warped disk geometries have been proposed to account for optical/IR (OIR) illumination effects seen in high-contrast images of Class II young stellar objects. Such two-sided shadows stand out in the outer disks of systems with a resolvable central cavity, i.e. in transition disks, as in HD 142527 (Marino et al. 2015), HD 100453 (Casassus 2016; Benisty et al. 2017; Long et al. 2017), DoAr 44 (Casassus et al. 2018), and HD 143006 (Benisty et al. 2018). The position and shape of the shadows place constraints on the orientation of the inner disk relative to the outer disk (Min et al. 2017), with consistent kinematics when resolved CO or HCO^+ rotational line data are available (Casassus et al. 2015a; Pérez et al. 2018).

An interesting consequence of tilted inner disks is that the outer rings are directly exposed to stellar radiations, except in the shadowed regions. If the shadow crossing time is larger or comparable to the gas cooling timescale, if $\Delta t_K \gtrsim \Delta t_c$, and depending on the extent of radiation diffusion from the rest of the disk, the gas and dust under the shadows may cool down appreciably, possibly resulting in a radio continuum drop. This seems to be the case in HD 142527, with a temperature drop of ∼30% in its northern shadow, as inferred from the grey-body analysis in Casassus et al. (2015b). Intriguingly, the existing ^{12}CO data in HD 142527 do not show any decrement, and the southern shadow is not matched by a continuum decrement as clear as in the northern shadow. Radio continuum counterparts to the OIR decrements have also been seen in DoAr 44 (Casassus et al. 2018), and in J1604-2130 (Mayama et al. 2018), even though in this source the shadows are variable (Pinilla et al. 2018). However, they are absent in other warped disks, such as in HD 143006 (Pérez et al. 2018) and in HD 100453 (van der Plas et al. 2019). Why is there such a broad variety in radio continuum responses under the shadows?

If $\Delta t_K \sim \Delta t_c$, the thermal lag in the shadowed gas and dust may be important, and the radio decrements could also lead the OIR shadows in the direction of Keplerian rotation, by an angular shift η_S. Can the position and shape of the temperature decrements constrain the outer disk mass? The depth of the radio decrements and the shift η_S may provide a measurement of the gas cooling timescale, which depends on the internal energy reservoir and hence on the gas mass. Quantitative predictions and limits based on measurement accuracies will require full-blown radiative transfer

★ E-mail: simon@das.uchile.cl

(RT) models that include the advection of internal energy in a prescribed velocity field. Meanwhile, Section 2 presents a one-dimensional model for the azimuthal temperature profile in the shadowed material, which Sec. 3 applies to the cases of HD 142527 and DoAr 44. Sec. 4 concludes on the two questions that motivate this letter.

2 MODEL FOR THE TEMPERATURE DROP OF SHADOWED MATERIAL

In a two-layer model for a passive disk (Chiang & Goldreich 1997), where the bulk mass is in the interior at a temperature T_g, the internal energy per unit surface in the disk is

$$U \approx \frac{1}{\gamma - 1} k \frac{\Sigma}{\mu m_p} T_g, \tag{1}$$

where Σ is the gas mass surface density, γ is the adiabatic index ($\gamma \approx 1.4$ for diatomic gas), k is the Boltzmann constant, $\mu = 2.3$ is the mean molecular weight and m_p is the proton mass. An approximation to cooling per unit area in the disk due to radiation from both disk surfaces is given by dust emission at a representative temperature T_d,

$$F_c \approx -2(1 - \exp(-\tau_P))\sigma T_d^4, \tag{2}$$

where $\tau_P = \Sigma \kappa_P$, and κ_P is the Planck-averaged absorption opacity (as in the deviation coefficients used by Dullemond et al. 2001). In the absence of shadows, the heating per unit area of the interior layer due to the stellar radiation transferred by the two surface layers can be written in terms of another temperature $T_\circ$,

$$F_h \approx 2(1 - \exp(-\tau_P))\sigma T_\circ^4. \tag{3}$$

The factor of $2(1 - \exp(-\tau_P))$ in Eq. 3 allows for $T_d = T_\circ$ in steady state, and in the absence of shadows, i.e. $T_\circ$ is the equilibrium temperature of the irradiated disk, as in Chiang & Goldreich (1997).

We will assume perfect thermal coupling of dust and gas, so that $T_g = T_d = T$ for the interior layer. The error involved in this approximation is within $\sim 20\%$, if it is similar to the difference in equilibrium temperature, evaluated at the midplane, for the small and large grain populations in the RT models used in Sec. 3. Under the isothermal approximation and with perfect thermal coupling, the cooling timescale can be defined as

$$\Delta t_c \equiv \left| \frac{U}{\dot{U}} \right| = \frac{1}{\gamma - 1} \frac{k\Sigma}{2(1 - \exp(-\tau_P))\sigma \mu m_p T_\circ^3}. \tag{4}$$

If $T_\circ$ drops suddenly to 0 at $\phi = 0$ when entering a shadow that extends to $+\infty$ along a straight line $\hat{s}$, then (keeping τ_P fixed at the unshadowed value),

$$T \approx T_\circ \left[1 + \frac{3R\phi}{v\Delta t_c} \right]^{-1/3}. \tag{5}$$

This approximation neglects cooling due to transport of mechanical energy, as in the work required in launching spiral arms (Montesinos et al. 2016). We assume that the power dissipated in spirals is similar to viscous heat dissipation, which is much less than that due to stellar radiation beyond a few au (e.g. Bitsch et al. 2013).

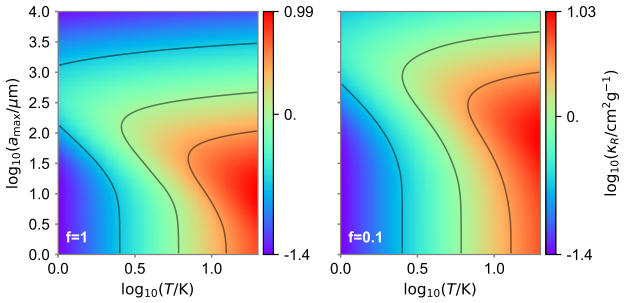

Figure 1. $\log_{10}(\kappa_R(a_{\max}, T))$ for two dust filling factors, $f = 1$ and $f = 0.1$. The 3 contours correspond to half the extrema of the colour bar and 0.

In optically thick media, with a gas density ρ, the transport of radiative energy density is due to diffusion, with a local flux

$$g_D = -\Lambda \frac{16\sigma T^3}{3\kappa_R \rho} \frac{dT}{ds}, \tag{6}$$

in direction $\hat{s}$. The Rosseland-mean opacity $\kappa_R(T)$ is given by

$$\frac{1}{\kappa_R(T)} = \frac{\int_0^\infty d\nu (1/\kappa_\nu) \partial B_\nu(T)/\partial T}{\int_0^\infty d\nu \partial B_\nu(T)/\partial T}, \tag{7}$$

in which κ_ν is the total mass opacity at frequency ν. The dimensionless control factor $\Lambda = 1$ for the Rosseland approximation, which requires a small photon effective mean-free-path (the net displacement due to scattering before absorption, Rybicki & Lightman 1986), i.e. $l_\star \ll H$ at the Wien wavelength. This condition can be approximated as $\tau_R \equiv \kappa_R \Sigma \gg 1$. In the applications below $0.01 < \tau_R < 27$, so in order to extend Eq. 6 to the optically thin transition we parametrise the control factor as in Dobbs-Dixon et al. (2010, their Eqs. 11 and 12).

The radii of cavities that can be resolved by direct imaging are $\gtrsim$30 au, where the equilibrium temperature in the midplane is usually < 100 K for Herbig Ae/Be and TTauri stars. The mass opacity κ_ν is therefore due to grains with water ice mantles. The available formulae for $\kappa_R(T)$ focus on higher temperatures and use a small maximum grain size, typically of $a_{\max} \sim 1\,\mu$m (e.g. Zhu et al. 2012). Since the large rings in Class II disks are associated with dust trapping, and possibly grain growth, we compute $\kappa_R(T, a_{\max})$ for a mix of water ice, silicates and graphite, with mass fractions of 0.4, 0.3, and 0.3, and an internal grain density $\rho_\bullet = 1.8\,\mathrm{g\,cm^{-3}}$. The analytical formulae in Kataoka et al. (2014) give the absorption and scattering cross sections $Q_\nu^{\rm abs}(a)$ and $Q_\nu^{\rm sca}(a)$ for spherical grains with radii a and filling factor f. For a power-law size distribution with exponent q,

$$\kappa_\nu = \frac{1}{f_{\rm gd}} \frac{3}{4 f \rho_\bullet} \frac{q+4}{a_{\max}^{q+4} - a_{\min}^{q+4}} \int_{a_{\min}}^{a_{\max}} da (Q_\nu^{\rm abs} + Q_\nu^{\rm sca}) a^{q+2}. \tag{8}$$

We set $q = -3.0$; this rather shallow value anticipates an application to transition disk rings, thought to undergo grain growth. The resulting Rosseland-mean opacities $\kappa_R(a_{\max}, T)$ are shown in Fig. 1, for a gas-to-dust mass ratio $f_{\rm gd} = 100$.

The total radiative flux in the azimuthal direction, i.e. in the direction $\hat{\phi}$, through a section of the disk at constant

ϕ, is

$$\mathcal{F}_\phi^D = \int dr \int dz g_D \approx \Delta R \int dz g_D, \quad (9)$$

for some small interval in stellocentric radius $\Delta R/R \ll 1$. Eq. 6 is applicable only to the disk interior, above the disk surface the radiation field points in the vertical direction, whereas in the low density limit Eq. 6 yields equal components in all directions. We assume that azimuthal radiation transport occurs at mid-plane densities, and that it extends over a vertical full-width-half-maximum,

$$\mathcal{F}_\phi^D \approx \Delta R \sqrt{2\pi} h R g_D|_{\rm midplane}, \quad (10)$$

for a hydrostatic and vertically isothermal disk with 1σ thickness HhR, where h is the 1σ disk aspect ratio. We checked this approximation *a-posteriori*, using the temperature profiles in the applications of Sec. 3 by modulating Eq. 6 with the hydrostatic Gaussian, finding that Eq. 10 underestimates Eq.9 by a factor $\sim 3 \pm 1$, which we chose to ignore. The net heating per unit disk surface is thus

$$F_\phi^D = -\frac{1}{\Delta R}\frac{\partial \mathcal{F}_\phi^D}{R\partial\phi} \approx \frac{\partial}{R\partial\phi} 2\pi H^2 \Lambda \frac{16\sigma T^3}{3\kappa_R \Sigma}\frac{\partial T}{R\partial\phi}. \quad (11)$$

Likewise, in the radial direction, the total flux of radiative diffusion through an arc length $R\Delta\phi$ is $\mathcal{F}_R^D \approx R\Delta\phi\sqrt{2\pi} H g_D|_{\rm midplane}$, and the neat heating per unit disk surface is

$$F_R^D = -\frac{1}{R\Delta\phi}\frac{\partial \mathcal{F}_R^D}{\partial R} = \frac{1}{R}\frac{\partial}{\partial R} R 2\pi H^2 \Lambda \frac{16\sigma T^3}{3\kappa_R \Sigma}\frac{\partial T}{\partial R}. \quad (12)$$

Radial diffusion turns out to be small compared to F_c. For a power-law disk with $H \propto R^{-\beta+\frac{3}{2}}$, $T \propto R^{-2\beta}$, $\Sigma \propto R^{-\gamma}$, a constant κ_R, $\beta = \frac{3}{8}$, setting $\Lambda = 1$ and at the peak surface density with $\gamma = 0$,

$$F_R^D = \frac{3\pi}{\kappa_R \Sigma}\frac{H^2}{R^2} 2\sigma T^4 \approx -0.1 F_c, \quad (13)$$

where the last approximation assumes $\kappa_R \Sigma \sim 1$ and $h \sim 0.1$.

For an incompressible Keplerian flow, at a fixed radius R and at constant velocity v in the direction $\hat{s} \parallel \hat{\phi}$, the net internal energy advected into a volume $d\mathcal{V} = \sqrt{2\pi} HR dR d\phi$ is $-v dR d\phi \frac{\partial U}{\partial \phi}$. The net heating per unit disk surface due to advection is thus

$$F_a = -\frac{v}{R}\frac{\partial U}{\partial \phi}, \quad (14)$$

This advection term is similar to that in the usual convective derivative. We neglect the random-walk delay associated to vertical diffusion, $\tau_\nu \times H/c$, which is of order a few days for IR photons.

Energy balance requires that

$$F_a + F_\phi^D + F_c + F_h = \frac{\partial U}{\partial t}, \quad (15)$$

where we have neglected radial diffusion. Following Eq. 3, we parametrise the heat source with an effective temperature T_h, so that $F_h(\phi) = 2(1 - \exp(-\tau_R))\sigma T_h^4(\phi)$. We replace τ_P by τ_R for simplicity, and Eq. 15 gives:

$$-\frac{1}{\gamma - 1} v\Sigma \frac{k}{\mu m_p}\frac{\partial T}{\partial \phi} + 2\pi H^2 \frac{16\sigma}{3\Sigma R}\frac{\partial}{\partial\phi}\left(\frac{f_{\rm gd}}{100}\frac{\Lambda T^3}{\kappa_R(T, a_{\rm max})}\frac{\partial T}{\partial\phi}\right) - 2\sigma(1 - \exp(-\tau_R))R(T^4 - T_h^4) = R\frac{\partial U}{\partial t}. \quad (16)$$

In steady state $\frac{\partial U}{\partial t} = 0$. We solve Eq. 16 with centered second-order finite differences, starting with a flat initial condition, and with periodic boundary conditions in $\phi \in [0, 2\pi]$.

We can now estimate a spatial scale associated to the smoothing effect of azimuthal radiation transport. For an infinite line along $s = R\phi$, in the absence of a heat source beyond the onset of a shadow at $s = 0$, without advection, and in the limit $\tau_R \gg 1$, Eq. 16 yields an exponential decay with e-folding length $L_D/H \approx \sqrt{f_{\rm gd}/(100\tau_R)} \ll 1$. However, if $\tau_R \ll 1$, assuming exponential decay yields $L_D/H \approx f_{\rm gd}/(100\tau_R)$, and radiation will strongly smooth out any temperature decrement. Likewise, away from the mid-plane, Eq. 6 suggests larger radiation flux at lower ρ. In the rarefied disk surface, e.g. where ^{12}CO rotational lines originate, the medium is optically thin and we expect qualitatively that the much larger photon mean-free path will smooth out the decrements.

3 APPLICATIONS

The shape of the shadows and $T_h(\phi)$ can potentially be constrained by observations and RT modeling. If we consider the details of $T_h(\phi)$ as fixed, as well as R and H, which are given by the disk structure, then in this simplified model the only free parameters governing the gas temperature as it crosses the shadows are: the disk surface density Σ, the gas-to-dust mass ratio $f_{\rm gd}$, the maximum grain-size $a_{\rm max}$, and the grain filling factor f.

3.1 HD 142527

The very lopsided ring of HD 142527 (Casassus et al. 2013) originates fairly optically thick mm-continuum in a stratified disk, so that the continuum profile is not axially symmetric, which hampers an isothermal description. A detailed comparison of the effect of advection under the shadows requires 3D RT models, as well as fine angular resolution data to infer the observed continuum temperature profile. Also, despite this source being the first in which sharp shadows from an inner disk were inferred, the precise location of the center of the shadows in the outer disk midplane has not yet been worked out. For now we use our simplified model to make qualitative predictions on the shape of the temperature decrements.

Under the shadows some radiative heating persists mainly due to IR thermal radiation from the inner disk. To guide the choice of the heat source $T_h(\phi)$, we examine the mean radiation intensity field in a parametric RT model meant to approximate the disk of HD 142527 at a distance of 140 pc, so somewhat less than the GAIA distance of 156 pc (hereafter the RT$_{1425}$ model, Marino et al. 2015; Casassus et al. 2015a,b). This model was computed with the RADMC3D package (Dullemond et al. 2015). The gas and the small grains are heated by UV radiation in the surface layers, while dust in the midplane will absorb transferred IR radiation. Using the RT$_{1425}$ model, we compute the mean radiation intensity $J(\phi)$ inside the cavity, right at the inner edge and in the midplane of the gaseous outer disk (so at a radius of 115 au). Fig. 2 compares the mean intensity field

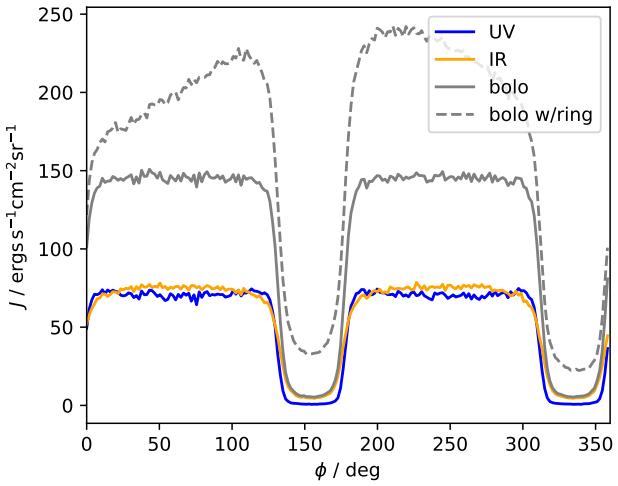

Figure 2. Mean intensity profile $J(\phi) = \int d\nu J_\nu(\phi)$, as a function of azimuth ϕ, at the outer edge of the cavity and in the midplane of a parametric model for HD 142527. We compare the UV/optical field, $J_{\rm UV}$ corresponding to $\lambda < 1\mu$m, with the IR field, $J_{\rm IR}$, for $\lambda > 1\mu$m, and with the bolometric field $J_{\rm bolo}$. All profiles are calculated in a model without outer disk, except for the dashed line, labeled 'w/ring', which corresponds to $J^{\rm w/ring}_{\rm bolo}$.

.

for $\lambda < 1\,\mu$m, $J_{\rm UV}$, with the mean field for $\lambda > 1\,\mu$m, $J_{\rm IR}$, and with the bolometric field $J_{\rm bolo}$, both in the presence and absence of the outer disk. About one third of $J^{\rm w/ring}_{\rm bolo}$ is thermal emission from the outer disk, hence its harmonic modulation in azimuth and its smoother profile under the shadows.

Since the dust responsible for the mm-continuum is thought to be trapped at the pressure maximum in the outer disk, radiation will be attenuated as it is transferred through the intervening material. This can be incorporated by setting the unshadowed temperature $T_\circ$ to the temperature of the larger grains (i.e. 1 mm – 1 cm). Since Eq. 16 accounts for outer disk radiation in the limited diffusion approximation, once we have set $T_\circ$, $T_h(\phi)$ should follow only radiation stemming from the star and the inner disk, which appears to be fairly square. The choice of a square profile for $T_h(\phi)$, with a total width ϕ_S for each shadow, and a floor temperature T_S, is also useful to estimate how the shape of the shadows maps into the temperature profile $T(\phi)$. We use hyperbolic tangents to round up the edges.

The temperature for the largest grains close to the northern shadow is observed to be $T_\circ \sim 27.5$ K (Casassus et al. 2015b). The floor temperature T_S can be inferred from the drop in radiation intensity, from $J_\circ$ in the unshadowed regions, to J_S under the shadows, $\frac{T_S}{T_\circ} \sim (J_S/J_\circ)^{1/4}$. Inspired by $J_{\rm bolo}(\phi)$ in Fig. 2, we set $T_S = 0.44\,T_\circ$ for RT$_{1425}$.

The peak gas surface density in the RT$_{1425}$ model is $\Sigma \sim 83\,{\rm g\,cm^{-2}}$, at $R = 155$ au, for a gas to dust mass ratio $f_{\rm gd} = 100$. The corresponding peak dust surface density is similar, within 50%, to that reported by Boehler et al. (2017) and Muto et al. (2015). In the analysis of Boehler et al. (2017) of CO isotopologue data, at the position of the peak in dust continuum, the gas-to-dust mass ratio is only $f_{\rm gd} = 1.7$, increasing to $f_{\rm gd} \sim 20$ in the direction of the minimum in continuum emission. For the northern shadow,

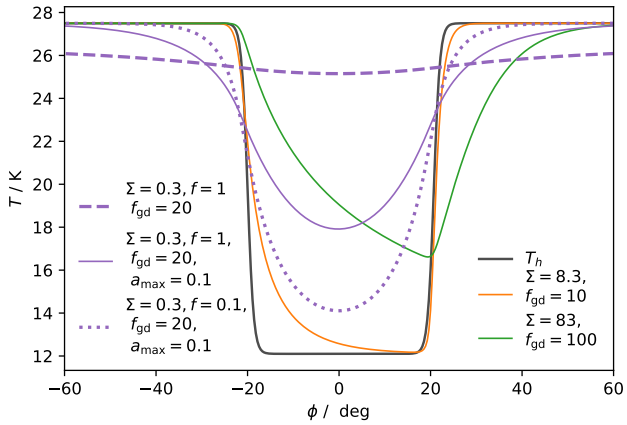

Figure 3. Example profiles for $T(\phi)$ that approximate HD 142527. All lines were computed for $a_{\rm max} = 1$ cm and $f = 0.1$ unless otherwise indicated in legends. The labels give surface density Σ in g cm^{-2}. Gas flows towards $+\hat{\phi}$.

there is general agreement in the literature on the dust surface density peak, around $\Sigma_d \sim 1\,{\rm g\,cm^{-2}}$. Since $\Sigma = f_{\rm gd}\Sigma_d$, we vary only $f_{\rm gd}$. The maximum grain size in the dust trap is at least $a_{\rm max} \sim 1$ cm (Casassus et al. 2015b), for which $\kappa_R = 0.05\,{\rm cm^2\,g^{-1}}$ if $f = 1$, and $\kappa_R = 0.32\,{\rm cm^2\,g^{-1}}$ if $f = 0.1$, so that $\tau_R \sim 4$ to 27. The cooling timescale is $\Delta t_c \sim 100 \times (f_{\rm gd}/100)$ yr. The shadow crossing time is $\Delta t_K \sim 152$ yr, for a stellar mass of $2.0\,{\rm M_\odot}$ (Mendigutía et al. 2014), and for a shadow width $\phi_S \sim 40$ deg. Thus, if $f_{\rm gd} \sim 100$ under the northern shadow, we expect dust to cool but not down to the floor temperature, since $\Delta t_c \sim \Delta t_K$. Since $L_D/H \sim 1/\sqrt{\tau_R} \lesssim 1$, the smoothing effect of radiative diffusion should have little impact. This scenario appears to be observed, given the temperature drop of ~30% reported by Casassus et al. (2015b).

Example solutions of Eq. 16, with the above parameters, are shown in Fig. 3. We see that for $f_{\rm gd} = 100$, radiative diffusion has no impact and the profile follows a cooling curve close to Eq. 5. A massive disk results in conspicuous shifts η_S between the temperature minimum and the centroid of the illumination pattern. For $f_{\rm gd} = 100$, $\eta_S = 19.1$ deg if $f = 0.1$ and $a_{\rm max} = 1$ cm, while for $f_{\rm gd} = 10$, $\eta_S = 14.4$ deg if $f = 1$ and $\eta_S = 16.2$ deg if $f = 0.1$.

For the southern shadow, in the RT$_{1425}$ model the maximum grain size that is not affected by azimuthal trapping is ~0.1 cm, for which $\kappa_R = 0.35{\rm cm^{-2}\,g^{-1}}$ if $f = 1$, and $\kappa_R = 1.1{\rm cm^{-2}\,g^{-1}}$ if $f = 0.1$ (both values at 27.5 K). We consider a single case for Σ: a gaseous disk mass contrast of ~3 as in Boehler et al. (2017), with $f_{\rm gd} \sim 20$ and $\Sigma \sim 0.3\,{\rm g\,cm^{-2}}$, so $\tau_R = 1.65$ if $f = 0.1$, and $\tau_R \sim 0.5$ if $f = 1$. Gas should cool much faster than in the northern shadow, since $\Delta t_c/\Delta t_K \gtrsim 10^{-2}$, but radiative diffusion should have more of an impact. Example solutions are shown in Fig. 3, where we also include a curve for $a_{\rm max} = 1$ cm and $f = 1$, for which $\tau_R \sim 0.015$. In this latter case the averaging effect of radiation transport almost completely smooths out the temperature decrement.

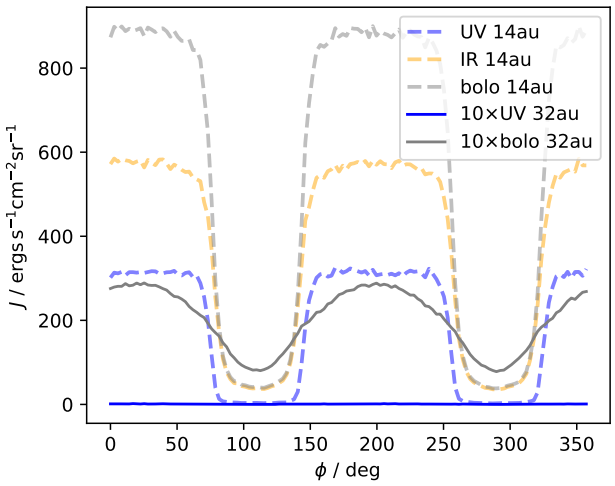

Figure 4. Mean radiation intensity $J(\phi)$ in a RT model for DoAr 44, without the outer disk. We plot $J(\phi)$ in the mid-plane and at two radii: at the edge of the gaseous cavity, so at $R_{\rm cavgas}$ = 14 au, and at the edge of the large-dust cavity, at $R_{\rm cavdust}$ = 32 au. The profiles at $R_{\rm cavdust}$ have been multiplied by 10. Conventions for the spectral domains follow from Fig. 2.

.

3.2 DoAr 44

The cavity in DoAr 44 is very different from HD 142527. In the parametric model of Casassus et al. (2018, hereafter $\rm RT_{DoAr44}$), the polarized-intensity image in H-band is reproduced with a gaseous cavity radius $R_{\rm cavgas}$ =14 au, while the continuum at 336 GHz corresponds to a larger cavity for the mm-sized dust, with $R_{\rm cavdust}$ =32 au. Thus, if due to shadowing, the continuum drops seen at 336 GHz, of ∼24%, result from a heat source profile $T_h(\phi)$ that has been substantially processed by intervening material, composed of gas and small dust (with radii $a < 1\mu$m in $\rm RT_{DoAr44}$). This is illustrated in Fig. 4, which plots the bolometric mean intensity field $J_{\rm bolo}$ at the edge of the gaseous cavity at $R_{\rm cavgas}$ and at $R_{\rm cavdust}$, in the absence of the outer disk. The broad and V-shaped decrements in $J_{\rm bolo}$ are very different from square profiles. Instead, for $T_{\rm h}(\phi)$ we use $J_{\rm bol}^{1/4}$, extracted at the edge of the large-dust cavity, i.e. at $R_{\rm cavdust}$ = 32 au, smoothed and normalized so that the peak temperature is that computed in the $\rm RT_{DoAr44}$ model (with the outer disk, and for the large dust population). The stellar mass for DoAr 44 is 1.3 $\rm M_\odot$ (Espaillat et al. 2010), and its distance in $\rm RT_{DoAr44}$ is 120 pc (now revised to 145.9 pc, Gaia Collaboration et al. 2016). The $\rm RT_{DoAr\,44}$ model suggests that the disk aspect ratio is $h \sim 0.08$ at $R_{\rm cavdust}$, coincident with the peak gas surface density of $\Sigma = 13\,{\rm g\,cm^{-2}}$ for $f_{\rm gd} = 100$, if $a_{\rm max} = 1$ mm.

As summarised in Fig. 5, the effect of advection is more important for a massive outer disk. In particular, the case for $f_{\rm gd} = 100$, $f = 1$, $a_{\rm max} = 1$ cm, with $\kappa_R(48\,{\rm K})$=0.06 $\rm cm^{-2}g$, corresponds to $\Sigma = 130\,{\rm g\,cm^{-2}}$ for the same mass in dust smaller than 1 mm as in $\rm RT_{DoAr\,44}$, and results in a large shift between the azimuthal position of the minimum in $T_{\rm h}$ and that of the minimum in T: $\eta_S = 16$ deg. The curves for $f_{\rm gd} = 100$, $a_{\rm max} = 0.1$ cm, and $f_{\rm gd} = 10$, $a_{\rm max} = 1$ cm, both correspond to $\Sigma = 13\,{\rm g\,cm^{-2}}$ (given the grain size exponent

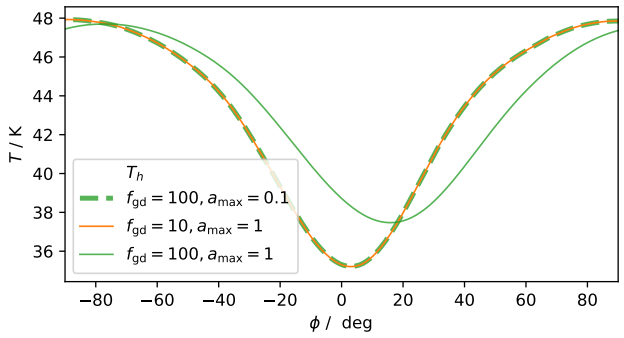

Figure 5. Example profiles $T(\phi)$ that approximate DoAr 44. All curves correspond to $f = 1$, and we vary the gas-to-dust ratio $f_{\rm gd}$, for $a_{\rm max} = 0.1$ cm and $a_{\rm max} = 1$ cm. The heat source $T_{\rm h}(\phi)$ is shown in black line. The direction of Keplerian rotation is towards $+\hat{\phi}$.

.

of $q = -3.0$), and $\eta_S = 2.9$ deg. A run for $f_{\rm gd} = 1$, $a_{\rm max} = 1$ cm ($\kappa_R(48\,{\rm K})$=0.40 $\rm cm^{-2}g$, not shown in Fig. 5), results in η_S = 0.36 deg. In all runs $\tau_R \gg 1$.

From the available observations Casassus et al. (2018) report $\eta_S = -2.8 \pm 0.9$ deg, which is a shift along the direction of rotation if the disk is rotating clock-wise (so if the northern side is the far side). With this direction of rotation the faint arc to the North-West (seen in polarized intensity, Avenhaus et al. 2018) can be seen as a trailing spiral arm. However, the substantial disk thickness in the H-band, and the finite inclination, result in a model $\eta_s^m = +3.0$ deg, as calculated with the $\rm RT_{DoAr\,44}$ predictions at native angular resolutions. After $uv-$plane filtering, the shift is $\eta_s^m = -1.3$ deg. If we take this offset of 4.3 deg as an indication of systematics, the observed value would be $+1.5 \pm 0.9$ deg. A very massive disk can thus easily be ruled out, and we can also discard at 5σ the cases with $f_{\rm gd} = 10$, $a_{\rm max} = 1$ cm, and $f_{\rm gd} = 100$, $a_{\rm max} = 0.1$ cm. A 3D RT model that incorporates advection, along with finer angular resolution data, could eventually refine these limits.

4 CONCLUSION

The midplane gas and dust cool when flowing across shadows cast by inner warps. In this letter we propose a simplified 1D model to explain the broad variety of temperature responses under the shadows, and to assess how the shape and depth of the temperature profiles depend on the outer disk mass. At low surface densities Σ, such that $\tau_R = \kappa_R\Sigma \ll 1$, or in the disk surface, radiation will smooth out the temperature decrements. In massive rings, such that $\tau_R \gtrsim 1$, the temperature minimum will be shifted in the direction of rotation relative to the centroid of the illumination pattern due to advection. This shift η_S is a probe of the gas-to-dust mass ratio for a given dust population.

Detailed applications to specific objects require the incorporation of advection in 3D radiative transfer. Meanwhile we report some of the prediction from our 1D model. The square illumination profile in HD 142527 allows to illustrate the impact of advection, even if in the isothermal approximation. A massive disk with $f_{\rm gd} > 10$ near the continuum peak

should result in a conspicuous shift, $14\,\mathrm{deg} \lesssim \eta_S \lesssim 20\,\mathrm{deg}$. A comparison with observations requires high angular resolution continuum data. In DoAr 44, the available observations allowed us rule out a massive disk with $\Sigma > 13\,\mathrm{g\,cm^{-2}}$ at 5σ, and given a standard dust population.

ACKNOWLEDGMENTS

The referee, Kees Dullemond, provided important and constructive warnings on the disk optical depth and the limits of the Rosseland approximation. We acknowledge further useful comments from Zhaohuan Zhu, Wladimir Lyra and Philipp Weber. Support was provided by Millennium Nucleus RC130007 (Chilean Ministry of Economy), FONDECYT grants 1171624 and 1151512, and by CONICYT-Gemini grant 32130007.

REFERENCES

Avenhaus H., et al., 2018, ApJ, 863, 44
Benisty M., et al., 2017, A&A, 597, A42
Benisty M., et al., 2018, preprint, (arXiv:1809.01082)
Bitsch B., Crida A., Morbidelli A., Kley W., Dobbs-Dixon I., 2013, A&A, 549, A124
Boehler Y., Weaver E., Isella A., Ricci L., Grady C., Carpenter J., Perez L., 2017, ApJ, 840, 60
Casassus S., 2016, PASA, 33, e013
Casassus S., et al., 2013, Nature, 493, 191
Casassus S., et al., 2015a, ApJ, 811, 92
Casassus S., et al., 2015b, ApJ, 812, 126
Casassus S., et al., 2018, MNRAS, 477, 5104
Chiang E. I., Goldreich P., 1997, ApJ, 490, 368
Dobbs-Dixon I., Cumming A., Lin D. N. C., 2010, ApJ, 710, 1395
Dullemond C. P., Dominik C., Natta A., 2001, ApJ, 560, 957
Dullemond C., Juhasz A., Pohl A., Sereshti F., Shetty R., Peters T., Commercon B., Flock M., 2015, RADMC3D v0.41 http://www.ita.uni-heidelberg.de/dullemond/software/radmc-3d/
Espaillat C., et al., 2010, ApJ, 717, 441
Gaia Collaboration et al., 2016, A&A, 595, A1
Kataoka A., Okuzumi S., Tanaka H., Nomura H., 2014, A&A, 568, A42
Long Z. C., et al., 2017, ApJ, 838, 62
Marino S., Perez S., Casassus S., 2015, ApJ, 798, L44
Mayama S., et al., 2018, ApJ, 868, L3
Mendigutía I., Fairlamb J., Montesinos B., Oudmaijer R. D., Najita J. R., Brittain S. D., van den Ancker M. E., 2014, ApJ, 790, 21
Min M., Stolker T., Dominik C., Benisty M., 2017, A&A, 604, L10
Montesinos M., Perez S., Casassus S., Marino S., Cuadra J., Christiaens V., 2016, ApJ, 823, L8
Muto T., et al., 2015, PASJ, 67, 122
Pérez L. M., et al., 2018, ApJ, 869, L50
Pinilla P., et al., 2018, ApJ, 868, 85
Rybicki G. B., Lightman A. P., 1986, Radiative Processes in Astrophysics
Zhu Z., Hartmann L., Nelson R. P., Gammie C. F., 2012, ApJ, 746, 110
van der Plas G., et al., 2019, arXiv e-prints,

This paper has been typeset from a TEX/LATEX file prepared by the author.